Electronic Supplementary Material (ESI) for ChemComm.

Supporting Information

Correlative imaging of ionic transport and electronic structure in practical $LiFePO_4$ electrodes

Mi Lu[a#], Fuda Yu[b#], Yongfeng Hu[c], karim Zaghib[d], Steen B. Schougaard[f]

Zhenbo Wang[b*], Jigang Zhou[c*], Jian wang[c*], John Goodenough[e]

- [a] *Key Laboratory of Functional Materials and Applications of Fujian Province, School of Materials Science and Engineering, Xiamen University of Technology, Xiamen, China, 361024;*
- [b] *School of Chemical Engineering, Harbin Institute of Technology, China. wangzhb@hit.edu.cn;*
- [c] *Canadian Light Source Inc., Saskatoon, Canada, S7N 2V3*
  E-mails: jigang.zhou@lightsource.ca; jian.wang@lightsource.ca
- [d] *Center of Excellence in Transportation Electrification and Energy Storage at Hydro Quebec, Canada*
- [e] *Texas Materials Institute ETC 9.102, The University of Texas at Austin, Austin, TX 78712, USA*
- [f] *Department for Chemistry, UQAM, 2101 rue Jeanne-Mance, Montreal, QC H1X 2J6, Canada*

1. SEM of LFP and charge/discharge curve of LFP

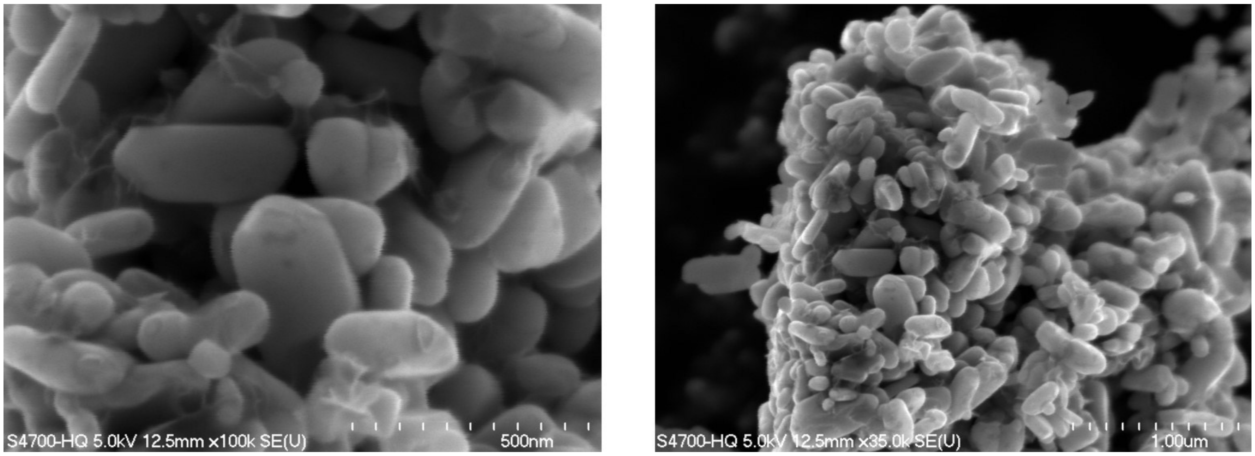

Fig. S1 (a) SEM of $LiFePO_4$ particles

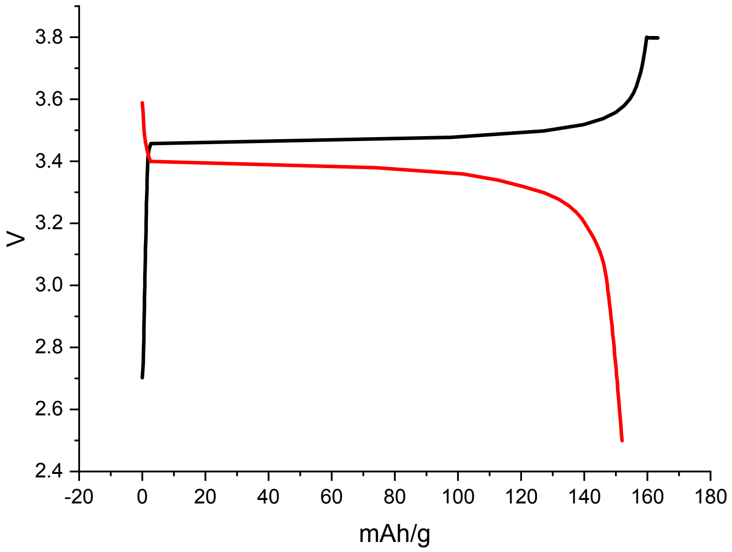

Fig. S1 (b) Charge and discharge curve of LFP under 1C

2. Details on STXM, PEEM and DFT calculation

2.1 STXM

LFP was released from a small piece cut of the electrode by ultrasonication with methanol. A drop of the dispensation was deposited onto a Si_3N_4 window and allowed it to dry before STXM. The SM STXM is equipped with a 25 nm outermost-zone zone plate (CXRO, Berkeley Lab), and the diffraction-limited spatial resolution for this zone plate is 30 nm. A 500 l/mm plane grating monochromator (PGM) was used for O K-edge and Fe L_3-edge measurements. The image pixel size was 25 nm with 1 ms dwell time per pixel. X-ray photon energy was calibrated using XANES of CO2 reported in the literature. Circularly polarized soft X-ray beam from the SM EPU was used to average out the in-plane polarization dependence of X-ray absorption if there is any such effect.

2.2 X-PEEM

X-ray beam was focused by an ellipsoidal mirror to ~20 µm spot on sample at a grazing incidence angle of 16°. Sample was biased at -20 kV with respect to the X-PEEM objective lens. Photocurrent from an Au coated Si_3N_4 window, located upstream of the X-PEEM main chamber, was measured for the incident beam intensity, and was used to normalize X-PEEM data. Chemical imaging and XANES spectra were obtained using field of view (FOV) image stacks (sequences) at the Fe L_3-edge, and O K-edges. The Pixel size of PEEM is about 40 nm. XANES obtained by PEEM is equivalent to spectra acquired by total electron yield (Surface Sciences 537 (2003)161-167).

2.3 Data analysis

STXM and X-PEEM data was analyzed by aXis2000 (available free for non-commercial applications at http://unicorn.mcmaster.ca/aXis2000.html). The O K-edge and Fe L_3-edge image stacks were appended together to form one whole stack, and then aligned and converted to absorbance (i.e. optical density). Such process assures the identical sample region to be chemically mapped at different absorption edges. Fe L-edge reference spectrum of Fe^{2+} was obtained from the original LFP while the reference spectrum of Fe^{3+} was from fully charged LFP. Chemical imaging of Li rich and Li poor phases was conducted for the Fe L-edge stack of the 50% DOD LFP to generate quantitative maps of Fe with different valance by fitting the stack with the reference spectra. The detailed lithium concentration in the bulk (STXM) and at the surface (X-PEEM) of lithium rich and lithium poor phases were determined by fitting the respective XANES spectra with Fe^{2+} ($Li_{1.0}FePO_4$) and Fe^{3+} standards (Li_0FePO_4). O K-edge XANES of bulk (STXM) and surface (X-PEEM) in lithium rich and lithium poor phases were extracted using the ROI obtained from mapping of Fe valence distribution.

2.4 DFT calculations

To understand the thermodynamics behavior of Li intercalation of $LiFePO_4$, configurations with the lowest electrostatic energy at different Li concentration were sampled and optimized by density functional theory (DFT) calculations via the CASTEP package. For all DFT calculations, the Perdew-Burke-Ernzerhof functional with spin-polarized generalized gradient approximation (GGA) was adopted to treat the exchange correlation energy with the projector augmented wave (PAW) potentials [1]. Due to the strongly correlated 3d-electrons, the rotationally invariant approach (DFT+U) was introduced, and the Hubbard U of Fe was set to 4.3 eV [2]. To ensure the energy convergence of 1.0×10^{-6} eV·atom^{-1} and the maximum force threshold of 0.01 eV·Å^{-1}, a plane wave basis with a cutoff energy of 500 eV and a Γ-centered Monkhorst-Pack mesh was applied. The atomic coordinates and lattice parameters of the calculation configurations (with a space group of *Pnma*) were fully relaxed.

3. Morphology mapping of $Li_{0.5}FePO_4$ electrode by STXM and X-PEEM

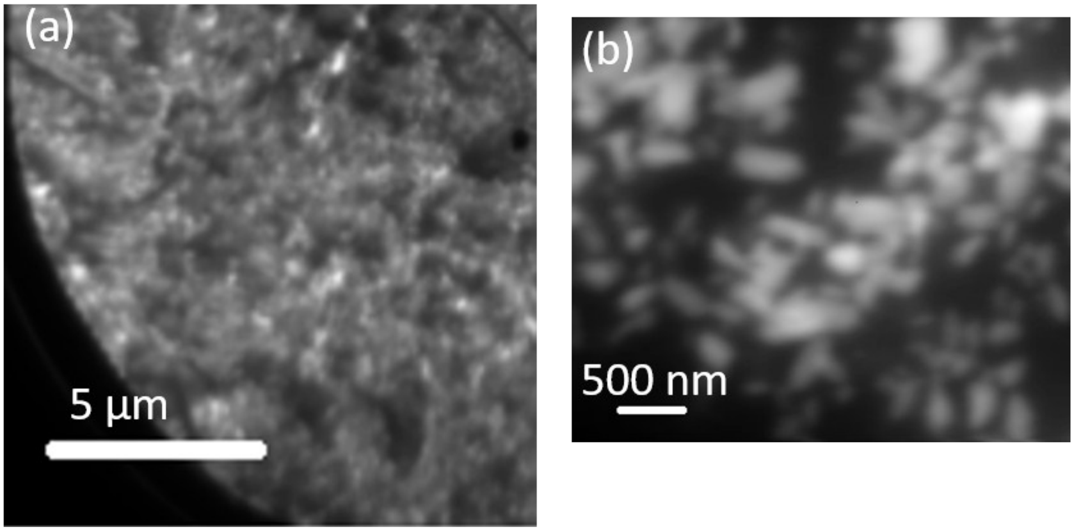

Fig.S2 Morphology mapping of $Li_{0.5}FePO_4$ electrode and LFP particles: (a) X-PEEM and (b) by STXM at Fe L_3-edge

4. Fe L_3-edge XANES spectra fitting for Li rich and Li poor in STXM and PEEM by of Fe^{2+} ($Li_{1.0}FePO_4$) and Fe^{3+} (Li_0FePO_4) standard spectra

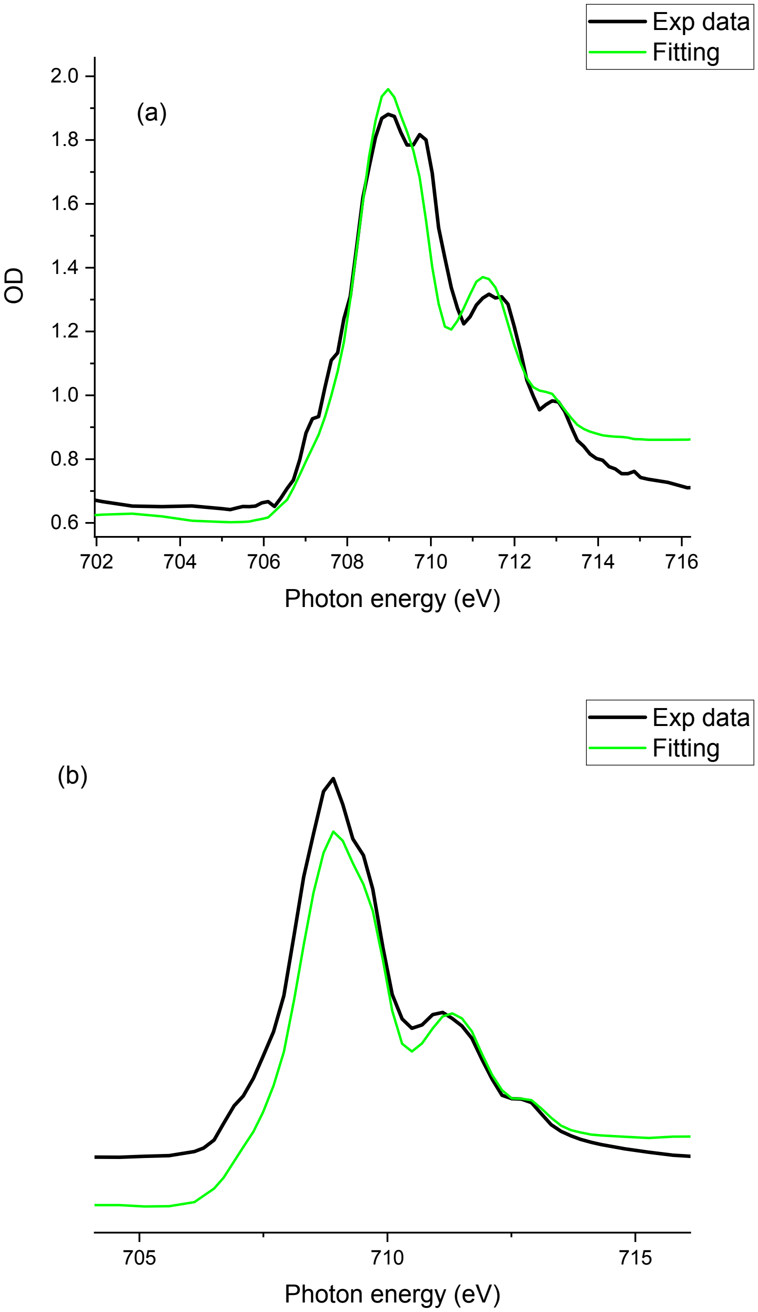

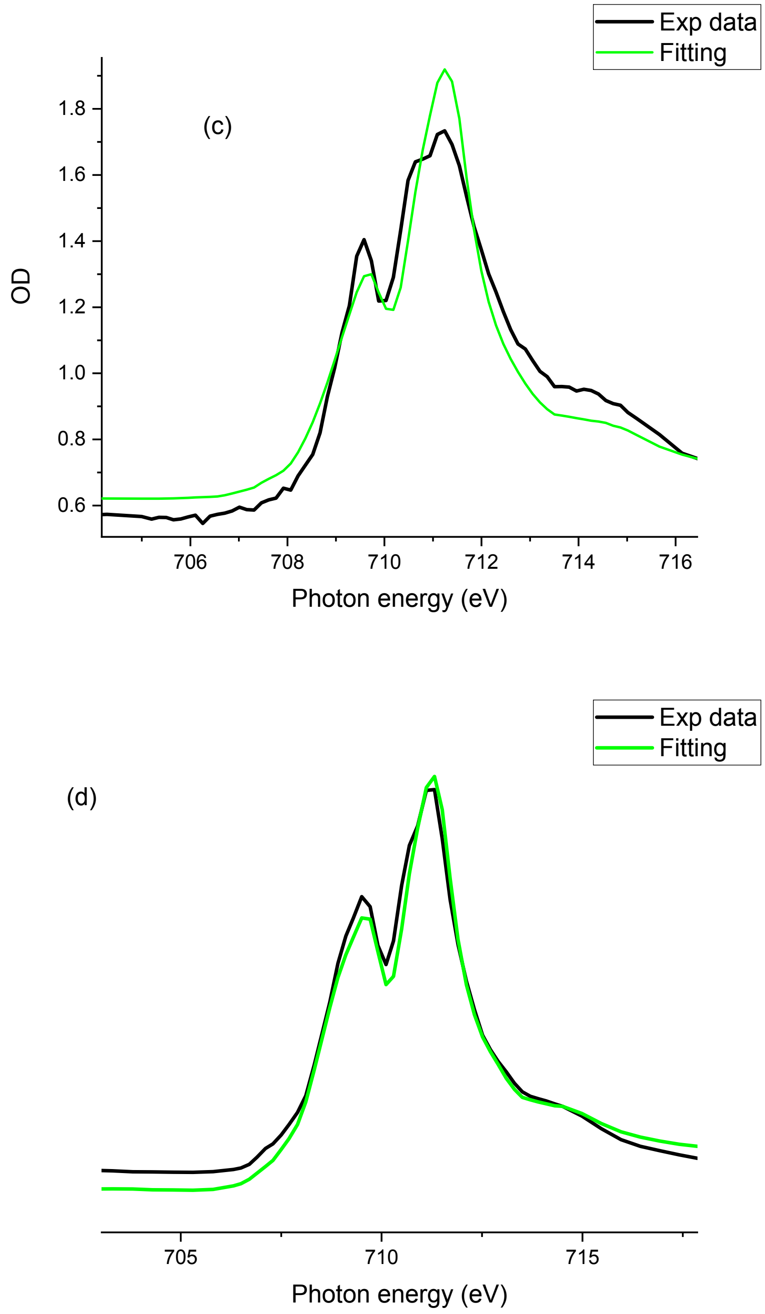

Fig. S3 Comparison of fitted and experimental Fe L-edge XANES of Li-rich in STXM (a), PEEM (b) and Li-poor in STXM (c) and PEEM (d).

5. Calculated stable endmember phases in LFP

The convex hull of formation energy is constructed at different Li concentrations and demonstrated **below**. It shows the four ground states of Li_xFePO_4 at x = 0, 0.9167, 0.9375 and 1. A two-phase reaction would occur at the regions from x = 0 to x = 0.9167, due to the minimum energy points located upward the convex hull.

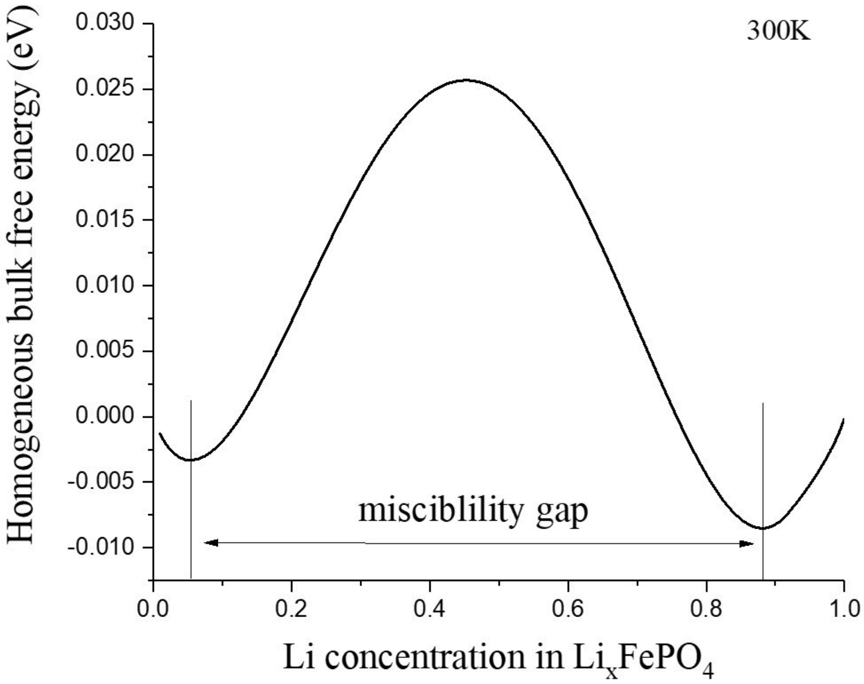

Fig. S4 The homogeneous bulk free energy as a function of Li concentration in Li_xFePO_4

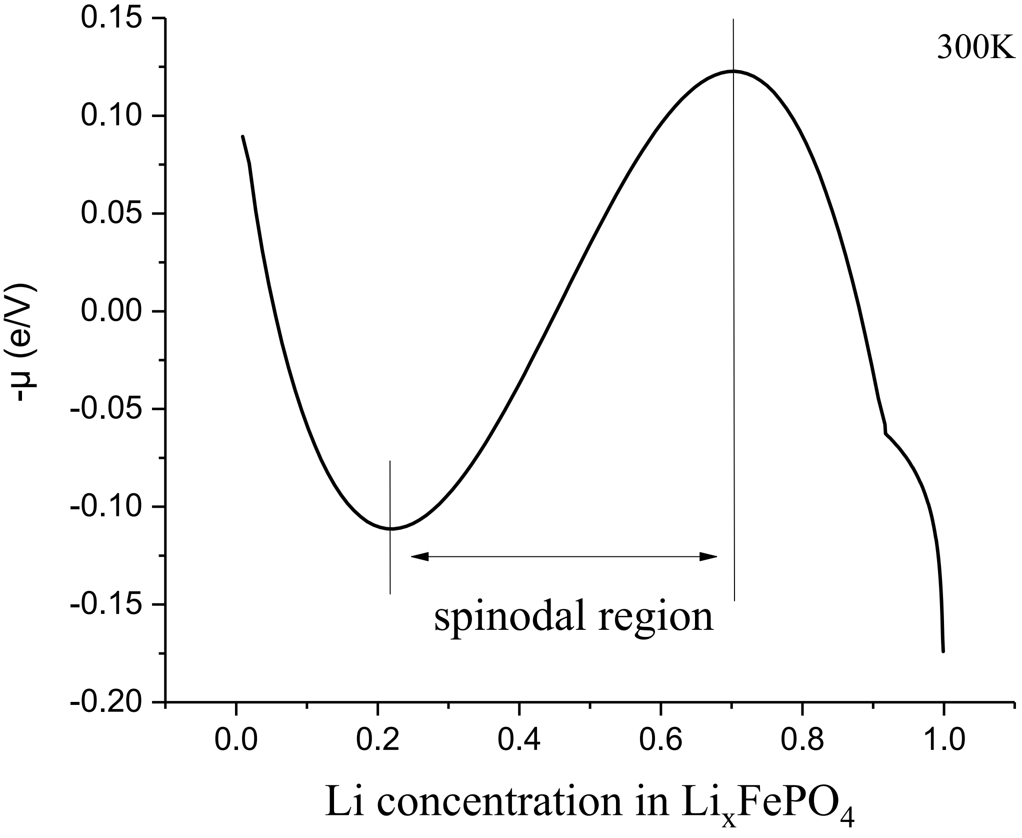

Fig. S5 The calculated chemical potential in Li_xFePO_4

6. Investigation of the electronic structure of LFP in the surface and in the bulk by DFT

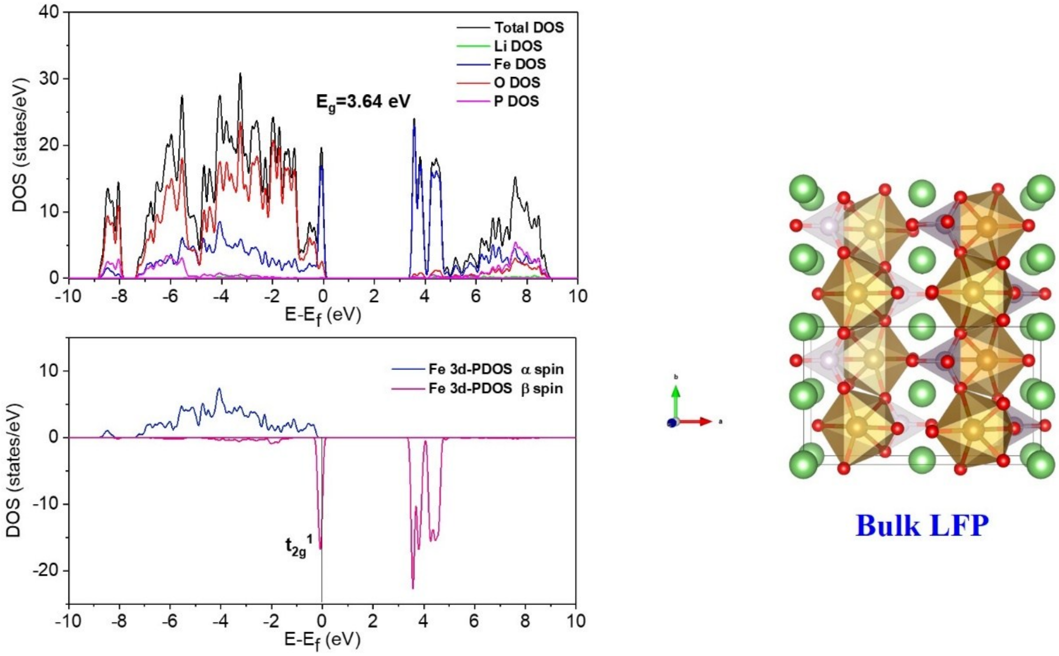

Fig. S6 The density state of bulk LFP As shown in **Fig. S6**, the valence band of bulk $LiFePO_4$ is dominated by the O-2p states, while the conduction band is mainly provided by Fe-3d states and hybrid with O 2p. The P, O, and Li atoms exhibit almost identical α and β spin channels, indicating zero net magnetic moments. While the 3d states of Fe species in α spin channel are fully occupied(t_{2g}^3), and only part of the t_{2g} states (t_{2g}^1) is filled in β spin channels. So, the spin configuration for Fe ions can attribute to $t_{2g}^4e_g^2$ with a theoretical magnetic moment of 4 μ_b. Moreover, the splitting of Fe-3d states leads to an energy gap (E_g) of about 3.64 eV, which is likely to determine the electronic conductivity of bulk $LiFePO_4$.

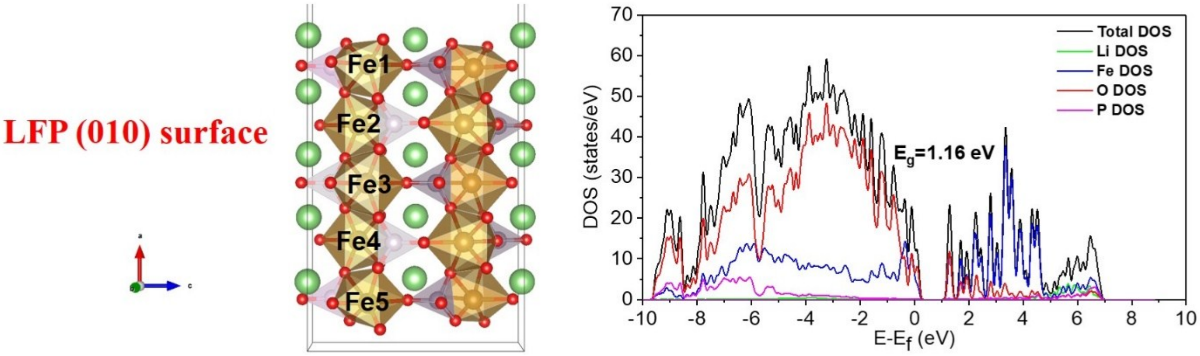

Fig.S7 The DFT geometry optimized configuration and DOS of LFP (010) surface

Fig. S7 shows the DOS of the $LiFePO_4$ (010) facet (with using a 13 Å vacuum layer to separate the periodic slabs), suggesting a much narrower band gap with 1.16 eV. This result may be associated with the different electronic structure on the surface compared with that of the bulk phase. In this surface model, the Fe1 and Fe5 atoms are located in the outermost layer, which refers to the Li-rich and delithiated state, respectively.

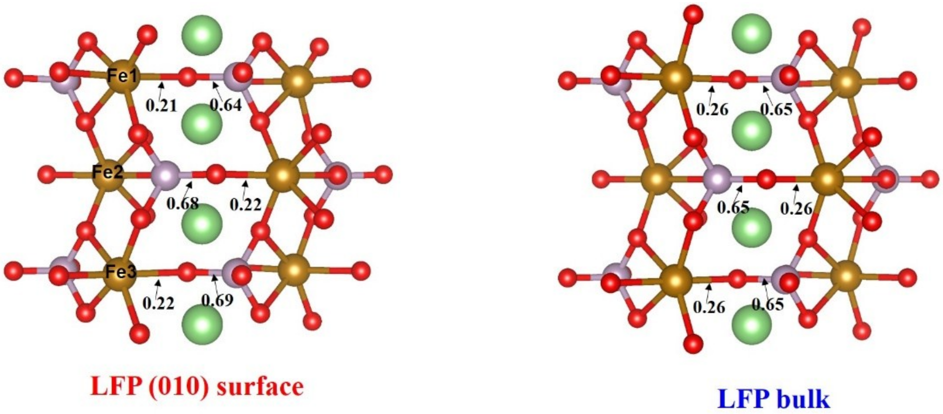

Fig. S8 The Mulliken bond populations of LFP (010) surface and bulk structure

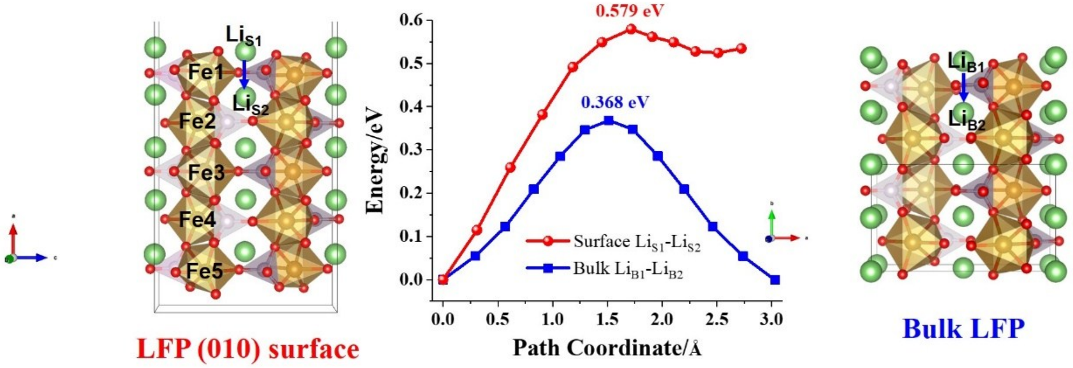

Fig.S9 The Li$^+$ migration activation energy with 010 trajectories for bulk and surface (010) LFP

Fig. S8 shows the Mulliken overlap populations for the bulk and surface LiFePO$_4$. The results suggest that the covalent interactions of Fe-O on the surface are weaker in contrast to the bulk structure. Based on the climbing-image nudged elastic band (CI-NEB) method, the activation barrier of Li$^+$ diffusion within the surface framework (Li$_{S1-S2}$, 0.579 eV) is higher than that of bulk (Li$_{B1-B2}$, 0.368 eV) (**Fig. S9**).

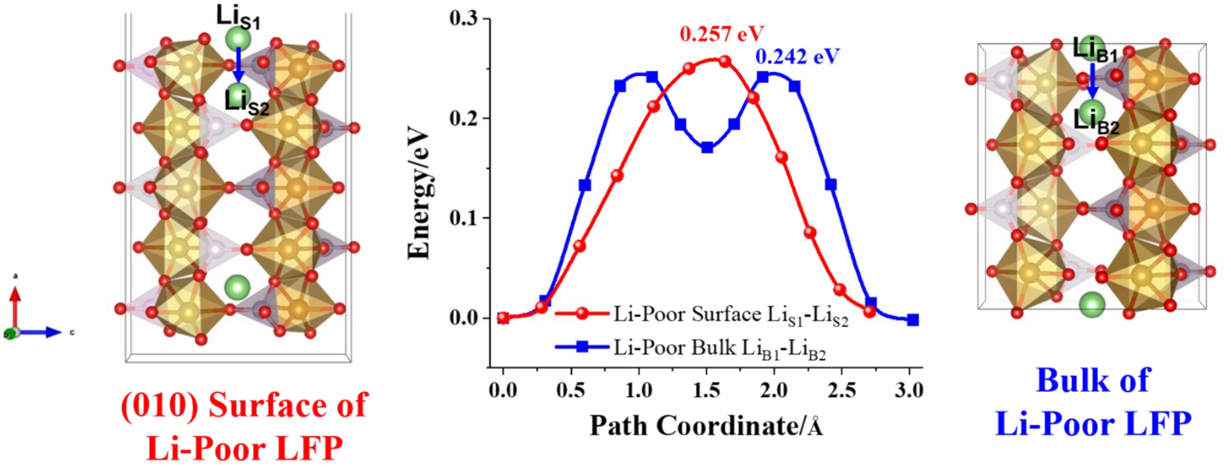

Fig. S10 The Li$^+$ migration activation energy with 010 trajectories for (010) surface and bulk of Li-poor LFP.

The calculated Li$^+$ migration activation energies for surface and bulk (0.257 and 0.242 eV) in Li-poor LFP ($Li_{0.3}FePO_4$) shown in Fig. S10 are both lower than those of the Li-rich LFP (0.579 and 0.368 eV) in Fig. S9, which suggests that Li$^+$ diffusion barriers are sensitive to the local environment changes induced by lithium vacancies, and such lithium vacancies likely reduce the electrostatic repulsion between the diffused Li$^+$ and its face-sharing species [3]. This indicates that the lithium transport between Li-poor and Li-rich structure is different, which is consistent with the observed Li concentration variation between the surface and bulk of both LFPs.

References

[1] S. J. Clark, M. D. Segall, C. J. Pickard, P. J. Hasnip, M. I. Probert, K. Refson, M. C. Payne, First principles methods using CASTEP. Zeitschrift für Kristallographie, 220 (2005) 567-570.

[2] K. Park, I. Park, H. Kim, G. Yoon, H. Gwon, Y. Cho, Y. S. Yun, J. Kim, S. Lee, D. Ahn, Y. Kim, H. Kim, I. Hwang, W. Yoong, K. Kang. Lithium-excess olivine electrode for lithium rechargeable batteries. Energy Environ. Sci., 9 (2016) 2902-2915.

[3] Dathar G. K. P., Sheppard D., Stevenson K. J., Henkelman G., Calculations of Li-ion diffusion in olivine phosphates, Chem. Mater., 23 (2011) 4032-4037.